Optics and Lasers in Engineering 203 (2026) 109793

Contents lists available at ScienceDirect

Optics and Lasers in Engineering

journal homepage: www.elsevier.com/locate/optlaseng

Automatic geometric calibration and unwarping of rotating line-scan imaging systems using elliptical distortion of circular patterns

Ling Cao [a,b], Wenxin Zhang [a], Daquan Feng [a], Wei Pan [b,c,*]

[a] College of Electronics and Information Engineering, Shenzhen University, Nanshan District, Shenzhen, Guangdong Province, China
[b] OPT Machine Vision, Department of R&D, 66 Xingfa South Road, Dongguan, Guangdong Province, China
[c] OPT Machine Vision Tech Co., LTD. Japan , Department of R&D, Aomi 2-7-4-735, Koto, Tokyo, Japan

ARTICLE INFO

Keywords:
Line-scan camera
Geometric calibration
Ellipse fitting
Sector-scan imaging
3D reconstruction
Circular calibration pattern

ABSTRACT

Rotating line-scan cameras and laser profilers operate under a sector-scan geometry, which introduces systematic geometric distortions in both 2D intensity images and 3D line-scan height profiles. This paper presents an image-driven geometric calibration and unwarping framework for such systems using a simple circular-hole calibration plate. Under sector-scan sampling, circular holes are projected as ellipses whose centers and aspect ratios encode the underlying rotation geometry. By exploiting this elliptical distortion, the proposed method estimates the rotation center and angular sampling characteristics without requiring encoders, mechanical measurements, or auxiliary sensors. A unified polar-to-Cartesian unwarping transformation is then applied to both 2D and 3D line-scan data. Experiments on real rotating line-scan systems show that the proposed approach effectively corrects sector-scan distortions, restores the geometric regularity of circular features in 2D images, and reduces rotational sampling artifacts in reconstructed 3D surfaces.

1. Introduction

Line-scan imaging systems form two-dimensional images by combining one-dimensional sensing with controlled motion. This imaging principle has been widely adopted in industrial inspection and precision metrology, particularly in scenarios that demand high spatial resolution along the scanning direction. Because the second image dimension is entirely determined by motion, geometric calibration plays a critical role in defining the image formation process and ensuring correct geometric interpretation.

Early studies on line-scan camera calibration were primarily developed under translational scanning configurations. In such systems, the relative motion between the camera and the object is linear, and the spatial relationship between successive scanlines remains uniform [1,2]. Under this assumption, various calibration strategies were proposed using planar or three-dimensional targets, enabling intrinsic and extrinsic parameters to be estimated through geometric constraints and optimization [3,4]. To improve robustness and deployment flexibility, subsequent works introduced auxiliary frame cameras or more complex calibration targets [5], and refined imaging models to account for non-ideal factors such as motion inclination and lens distortion under linear scanning conditions[6,7].

Beyond translational motion, rotational scanning is widely adopted in industrial inspection and measurement applications. Typical scenarios include the inspection of cylindrical workpieces, rotary surface profiling, and panoramic imaging of objects with rotational symmetry [8,9]. Rotational motion provides an efficient means to cover large fields of view or curved surfaces, but also introduces fundamentally different sampling characteristics. Several studies have therefore investigated calibration strategies for rotating systems, focusing on rotation axis modeling, eccentricity estimation, and kinematic error compensation to improve measurement reliability [10,11]. These works highlight the practical importance of calibration in rotating line-scan and laser-based systems deployed in industrial environments.

From a broader perspective, sector-scan or polar sampling geometries have long been studied in ultrasound imaging. In that domain, scan conversion techniques are commonly used to transform polar-sampled data into Cartesian space for visualization and analysis [12]. However, the scanning geometry is typically assumed to be known and fixed, and research efforts mainly focus on interpolation accuracy and real-time implementation, rather than on geometric calibration itself.

Within optical measurement and calibration research, related efforts have addressed rotation center estimation and eccentricity compensation in rotating systems [13,14]. In parallel, circular targets and

* Corresponding author.
E-mail address: vpan@foxmail.com (W. Pan).

https://doi.org/10.1016/j.optlaseng.2026.109793
Received 9 February 2026; Received in revised form 30 March 2026; Accepted 7 April 2026
Available online 23 April 2026

ellipse fitting have been widely employed in optical calibration, for example to recover light-plane parameters [15] or to establish task-specific measurement models based on fitted ellipse geometry [16]. These studies demonstrate the effectiveness of circular patterns and ellipse analysis; however, existing approaches typically rely on complex calibration setups or specialized targets. Moreover, ellipse deformation is often treated as a secondary effect caused by projection or misalignment, rather than being directly exploited as a carrier of scanning geometry.

As a result, despite the widespread use of rotating line-scan systems in industrial practice, a simple, image-driven calibration method that directly recovers sector-scan geometry remains lacking. In particular, existing approaches do not explicitly exploit the fact that, under rotational scanning, circular patterns naturally undergo sector-scan distortion and appear as ellipses in the image. The geometric relationship between circles and ellipses induced by rotational sampling has not been systematically formulated into a concise and deployable calibration framework.

In this work, we address this gap by proposing an ellipse-distortion-based geometric calibration and unwarping framework for rotating line-scan imaging systems. The proposed method exploits the elliptical deformation of circular-hole patterns induced by sector-scan sampling to recover key scanning geometry parameters directly from image-domain observations, without relying on encoders, auxiliary sensors, or mechanical measurements. The recovered geometry further supports a unified polar-to-Cartesian unwarping transformation, which is applicable to both 2D line-scan intensity images and 3D laser-based height profiles. In addition, we design geometry-driven evaluation metrics to quantitatively assess the effectiveness of the unwarping process without requiring external ground-truth measurements. In broader robotic vision systems, 3D point acquisition is often achieved through multi-view stereo, structured-light sensing, or multi-sensor fusion frameworks [17–20]. These approaches emphasize reconstruction completeness and robustness, but typically require multiple sensors, synchronization, and explicit geometric calibration. In contrast, the proposed method estimates the scanning geometry directly from image-domain distortions in a single rotating line-scan system. This avoids the need for multi-view observations, encoder signals, or additional sensing devices, making the method particularly suitable for compact industrial inspection systems.

The remainder of this paper is organized as follows. Related work is reviewed in Section 2. The proposed calibration and unwarping framework is described in Section 3. Experimental validation on real rotating line-scan camera and laser profiler systems is presented in Section 4, followed by results and discussion in Section 5. Conclusions are drawn in Section 6. The main contributions of this work are summarized as follows:

- We propose an ellipse-distortion-based geometric calibration framework for rotating line-scan imaging systems, enabling image-domain estimation of the rotation center and angular sampling characteristics under sector-scan geometry.
- Unlike existing approaches that rely on encoders, auxiliary sensors, or explicit mechanical measurements, the proposed method infers scanning geometry directly from distorted circular patterns, significantly simplifying system deployment while maintaining robustness.
- A unified polar-to-Cartesian unwarping model is developed and shared across both 2D line-scan imagery and 3D laser-based height profiles, allowing consistent correction within a single geometric formulation.
- Geometry-driven evaluation metrics are designed to quantitatively assess the effectiveness of sector-scan unwarping based on shape regularity and structural consistency, without requiring external ground-truth references.

2. Related work

This section reviews prior studies related to line-scan camera calibration, rotating and sector-scan imaging systems, circular and elliptical feature-based geometric inference, robust ellipse fitting and regression, and calibration of 3D laser profilometry. The limitations of existing approaches under sector-scan sampling are highlighted to motivate the proposed image-driven calibration framework.

2.1. Calibration of line-scan cameras

Most existing calibration methods for line-scan cameras assume that image formation is driven by linear translational motion. Under this assumption, classical approaches extend planar target calibration from area-scan cameras to the line-scan setting by exploiting known motion directions and well-defined geometric patterns [3,4,21]. Intrinsic parameters, extrinsic pose, and motion direction are typically estimated using optimization-based formulations.

To improve calibration feasibility in practical systems, several methods introduce additional constraints or auxiliary sensing. A common strategy employs a pre-calibrated area-scan camera to assist line-scan calibration by establishing indirect image–world correspondences [5]. Other works design specialized calibration targets with strong geometric constraints, enabling static calibration without explicit motion modeling [22]. While effective, these approaches increase system complexity and still fundamentally rely on translational sampling assumptions.

More recent studies extend dynamic imaging models to better describe non-ideal translational scanning conditions, such as eccentricity, motion inclination, and lens distortion [23]. These methods improve modeling fidelity under rectilinear motion, but remain developed within a translational scanning framework and are not directly applicable to rotating or sector-scan imaging, where distortions arise from angular sampling rather than linear displacement.

2.2. Rotating and sector-scan imaging systems

Sector-scan imaging has been extensively studied in application domains where data are naturally sampled in polar coordinates and subsequently transformed into Cartesian space for visualization. Typical examples include ultrasonic imaging systems, in which scan-conversion algorithms have been developed to reduce interpolation artifacts and enable real-time display [12,24]. These methods generally assume that the scanning geometry is precisely known and fixed, and therefore focus on resampling efficiency rather than geometric calibration or image-domain recovery of unknown scanning parameters.

In optical measurement, rotating line-scan systems have been explored for panoramic observation and three-dimensional reconstruction. Early systems relied on stereo configurations composed of multiple line-scan cameras to recover 3D geometry under controlled rotational motion [8]. More recent approaches predominantly adopt rotating laser triangulation sensors or structured-light scanners, where geometric calibration is achieved by explicitly modeling the rotation axis and system kinematics [9,25]. These methods typically depend on known angular motion, mechanical measurements, or rotary encoders, and mainly target accurate 3D reconstruction rather than image-domain geometric correction.

From a metrology and industrial inspection perspective, rotating laser line scanners have been widely applied to surface measurement, gear inspection, and additive manufacturing evaluation [13,26]. Such studies generally assume pre-calibrated scanning geometry and do not address geometric calibration under unknown rotational or sector-scan imaging conditions.

2.3. Circular and elliptical feature-based geometric inference

Circular and elliptical features are widely used as robust geometric primitives in optical and vision systems. In polar-coordinate alignment tasks, image-based circle center localization is often adopted to estimate rotary axis alignment and correct axis–optical misalignment [27]. In rotating measurement systems, a substantial body of work analyzes

eccentricity or center-of-rotation (COR) errors and compensates them using explicit geometric models or calibration procedures [10,11].

For rotating 3D scanners, boresight and assembly misalignments are often estimated by exploiting scene constraints such as planar surfaces, aiming at reducing systematic errors in Cartesian reconstruction [14]. Elliptical analysis has also been employed in image-based tracking of rotating structures, where ellipse parameters are used to correct misalignment or stabilize motion estimation [28].

In the context of structured-light and camera calibration, circular targets are frequently used, and ellipse fitting is combined with projection geometry to recover system parameters or compensate eccentricity [15,29,30]. However, in these works, ellipses are primarily treated as projection-induced shapes or local measurement primitives. They do not analyze how ellipse parameters vary systematically under sector-scan sampling, nor do they exploit such distortions to infer scanning geometry directly.

2.4. Robust ellipse fitting and regression methods

Accurate ellipse fitting under noise and outliers is a long-standing problem in computer vision. The classical direct least-squares formulation proposed by Fitzgibbon et al. [31] remains a widely used baseline. To improve robustness, RANSAC-based approaches and their variants have been extensively studied in robotic and geometric estimation contexts [32].

Recent works propose adaptive RANSAC strategies and multi-scale smoothing to improve ellipse fitting accuracy under noise, partial occlusion, and outliers [33,34]. Learning-based ellipse detection methods have also been introduced to further enhance detection precision in challenging imaging conditions [35]. These advances provide valuable tools for improving measurement robustness, but they are not designed to recover global sector-scan geometry or angular sampling characteristics.

2.5. Calibration for 3D laser profilometry

From a metrology viewpoint, calibration of laser triangulation scanners often emphasizes systematic error correction and uncertainty evaluation using reference artifacts [36,37]. Such procedures assume that the scanning geometry is already defined and focus on traceability and performance assessment.

For line-structured light profilometry, many methods calibrate the light plane or build task-specific mappings. Representative approaches use circular targets to recover the light plane with high precision or to compensate task-dependent geometric errors [16]. In robotic and multi-sensor configurations, hand–eye calibration and joint optimization of multiple profilers are commonly employed [38–40]. These approaches typically rely on explicit kinematic modeling and mechanical constraints, and do not infer scanning geometry from image-domain distortions.

From a broader perspective, 3D data acquisition and geometric reconstruction in robotic vision systems are commonly achieved through multi-view stereo, structured-light sensing, and multi-sensor fusion frameworks. These approaches are widely used in robotic navigation, industrial inspection, and autonomous systems, where multiple sensing modalities are combined to improve reconstruction accuracy and robustness [17,18].

Recent developments also emphasize distributed sensing and intelligent data management for robotic swarms, where 3D optical sensors and dynamic triangulation are integrated with communication and data fusion strategies to enhance perception capabilities in complex environments [19,20]. While these methods focus on large-scale perception and multi-sensor cooperation, they typically assume pre-calibrated sensor geometry and do not address geometric calibration in rotating line-scan imaging systems.

In contrast, the proposed method directly infers scanning geometry from image-domain distortions observed in a single rotating line-scan system. This eliminates the need for multi-view fusion, external sensors, or encoder measurements, and enables unified calibration for both 2D intensity images and 3D height profiles.

2.6. Summary and positioning of this work

Based on the above review, the main limitations of existing approaches can be summarized as follows:

- most line-scan camera calibration methods are developed under translational motion assumptions and cannot directly handle sector-scan distortions;
- many rotating scanner calibration approaches depend on encoder measurements or explicit mechanical knowledge, which increases system complexity;
- circular and elliptical features are widely used, but their systematic distortion under sector-scan imaging has not been exploited for geometric inference;
- calibration frameworks for 2D line-scan images and 3D laser-based height maps are usually designed separately and do not share a unified imaging model.

This paper addresses these gaps by introducing, to the best of our knowledge, the first calibration method that:

1. exploits elliptical distortions of circular-hole patterns to infer the rotation center and angular sampling;
2. provides a purely image-based, encoder-free solution;
3. constructs a global unwarping transformation valid for both 2D intensity images and 3D height maps;
4. enables robust calibration even with modest angular coverage and limited ROI observations.

This positions the proposed method as a general and unified solution for geometric correction of rotating line-scan imaging systems under sector-scan sampling.

3. Proposed method

The proposed method estimates the geometric parameters of a rotating line-scan system from the elliptical distortions of circular-hole patterns. It consists of five stages: (1) modeling the sector-scan imaging geometry, (2) ROI extraction and robust ellipse fitting, (3) estimation of the rotation center via aspect-ratio measurements, (4) estimation of the angular sampling rate from ellipse center positions, and (5) construction of a unified polar-to-Cartesian unwarping transformation for both 2D images and 3D height maps.

3.1. System overview and assumptions

Fig. 1 illustrates the system setup and the resulting sector-scan image formation. Due to line-by-line acquisition during stage rotation, circular holes on the calibration plate are warped into ellipses, which serve as the geometric cues for subsequent parameter estimation.

The proposed formulation relies on several geometric assumptions. First, the rotation axis is assumed to be perpendicular to the imaging plane, ensuring that circular features are observed as ellipses under rotational scanning. Second, the acquired scan line is assumed to pass through the center of the calibration disk. These assumptions establish stable geometric relationships for ellipse-based parameter estimation. Deviations from these conditions may introduce additional parameters and reduce estimation accuracy. The effects of such deviations are further discussed in Section 5.5.

3.2. Ellipses as geometric carriers in sector-scan imaging

In the proposed framework, ellipses are not treated merely as local image primitives, but as geometric carriers that encode the global sector-scan sampling geometry. While individual ellipse parameters may be

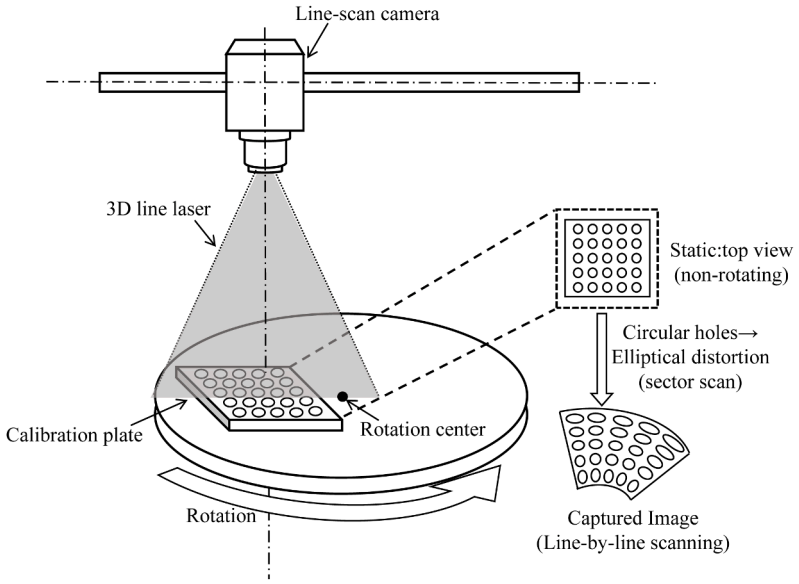

Fig. 1. System configuration and sector-scan image formation. A line-scan camera is mounted above a rotating stage. A square circular-hole calibration plate is placed off-center on the stage. During rotation, line-by-line scanning produces a sector-shaped image in which circular holes are distorted into ellipses.

perturbed by noise, partial occlusion, or imperfect edge localization, their collective distribution exhibits stable trends that enable regression-based estimation of the global calibration parameters.

This differs from classical calibration pipelines that rely on high-precision feature correspondences. Here, geometric information is embedded in the statistical consistency among multiple ellipses rather than any single measurement.

3.3. Imaging geometry of rotating line-scan systems

Let the unknown rotation center in the acquired image be (x_c, y_c). Each image row corresponds to an angular position of the rotating stage. Let k be the angular sampling rate (rad/row). For a pixel at (x, y), we define the sector-scan coordinates w.r.t. the rotation center as

$$r = x - x_c, \tag{1}$$

$$\theta = k\,(y - y_c). \tag{2}$$

Under this mapping, circular holes on a planar calibration plate appear as ellipses in the captured image (see Fig. 1). The goal is to estimate (x_c, y_c) and k directly from the observed ellipses.

3.4. ROI extraction and preprocessing

Reliable ellipse fitting requires accurate extraction of boundary points for each hole. The preprocessing stage includes: (1) global-to-local ROI localization, (2) adaptive segmentation, (3) gradient-based subpixel edge localization, and (4) outlier suppression and contour regularization.

3.4.1. Global hole localization

Let $I(x, y)$ be the captured line-scan image. We compute a smoothed version

$$I_s = G_\sigma * I,$$

where σ is chosen to suppress line-scan noise while preserving boundaries. Candidate hole regions are detected by local intensity variance

$$V(x, y) = \mathrm{Var}(I_s(\mathcal{N}_w(x, y))),$$

where $\mathcal{N}_w$ is a $w \times w$ window. Connected components satisfying $V(x, y) > \tau_v$ are treated as coarse ROIs.

3.4.2. Adaptive threshold segmentation

Within each ROI Ω_i, hole interiors are segmented using an adaptive threshold

$$T_i = \mu_i - \lambda\sigma_i,$$

where μ_i and σ_i are the mean and standard deviation of I_s in Ω_i. Binary segmentation is defined as

$$B_i(x, y) = \begin{cases} 1, & I_s(x, y) < T_i, \\ 0, & \text{otherwise.} \end{cases}$$

Morphological opening is applied to reduce isolated noise.

3.4.3. Contour extraction and gradient-based edge localization

External contours are extracted via border-following. For each contour pixel (x_j, y_j), we refine it using the local gradient $\nabla I_s = (I_x, I_y)$. Let $\mathbf{n}_j = \nabla I_s / \|\nabla I_s\|$ be the normalized gradient direction. A subpixel boundary estimate (x'_j, y'_j) is obtained by 1D interpolation along $\mathbf{n}_j$, e.g., by locating a zero-crossing of the second directional derivative or an equivalent edge-localization criterion.

3.4.4. Outlier suppression and contour regularization

Raw contour points may include illumination artifacts, specular reflections, partial occlusion, or stripe noise. We fit a preliminary ellipse and remove outliers using a robust distance criterion (e.g., Mahalanobis distance) and then refit using the refined set.

3.4.5. Noise model

We assume additive image noise arising from sensor readout noise, laser speckle, and surface reflectivity variations commonly observed in laser line-scan imaging systems:

$$I(x, y) = I_0(x, y) + \eta(x, y), \quad \eta \sim \mathcal{N}(0, \sigma_n^2),$$

which induces approximately Gaussian perturbations on extracted edge points:

$$(\tilde{x}_j, \tilde{y}_j) = (x_j, y_j) + (n_{x,j}, n_{y,j}), \quad n_{x,j}, n_{y,j} \sim \mathcal{N}(0, \sigma_e^2).$$

This model is used for uncertainty propagation in subsequent estimation.

3.5. Direct least-squares ellipse fitting

Each ROI contour is fitted to a general conic

$$Ax^2 + Bxy + Cy^2 + Dx + Ey + F = 0, \tag{3}$$

with the ellipse condition

$$B^2 - 4AC < 0. \tag{4}$$

Following Fitzgibbon et al. [31], the conic parameters $\mathbf{p} = (A, B, C, D, E, F)^\top$ are estimated by a constrained least-squares formulation. The geometric ellipse parameters are then recovered as

$$(c_{x,i}, c_{y,i}), \quad r_{x,i}, r_{y,i}, \quad \alpha_i,$$

representing center, semi-axes, and orientation. Ellipses with large residuals or unreasonable aspect ratios are rejected. Such cases typically arise from incomplete contours, spurious edges, or fitting instability under low signal-to-noise conditions. Extremely elongated or nearly degenerate ellipses are excluded to ensure stable geometric parameter estimation.

3.6. Uncertainty propagation of ellipse measurements

Ellipse fitting is the primary source of uncertainty. Let $\mathbf{p}$ denote the fitted conic parameters and $\mathbf{q} = (c_x, c_y, r_x, r_y)^\top$ be the geometric parameters, related by $\mathbf{q} = \mathbf{g}(\mathbf{p})$. To first order, the covariance of $\mathbf{p}$ is approximated by

$$\mathbf{C_p} \approx \sigma_e^2 (\mathbf{M}^\top \mathbf{M})^{-1},$$

and the covariance of $\mathbf{q}$ follows from linear error propagation

$$\mathbf{C_q} = \mathbf{J_g} \mathbf{C_p} \mathbf{J_g}^\top,$$

where $\mathbf{J_g}$ is the Jacobian of $\mathbf{g}(\cdot)$. The uncertainty of the aspect ratio

$$\rho_i = \frac{r_{x,i}}{r_{y,i}}$$

is obtained by standard variance propagation:

$$\mathrm{Var}(\rho_i) = \frac{1}{r_{y,i}^2}\mathrm{Var}(r_{x,i}) + \frac{\rho_i^2}{r_{y,i}^2}\mathrm{Var}(r_{y,i}) - \frac{2\rho_i}{r_{y,i}^2}\mathrm{Cov}(r_{x,i}, r_{y,i}). \tag{5}$$

3.7. Ellipse geometry and linearized measurement model

Under the sector-scan mapping (1)–(2), a circular hole becomes an ellipse. In practice, the aspect ratio varies monotonically with the hole's angular position. To connect this geometric behavior to a regression-ready measurement model, we introduce a 1D ordering variable s_i such that θ_i varies approximately affinely with s_i over the calibration field of view:

$$\theta_i \approx \kappa\, s_i + \theta_0. \tag{6}$$

In our setup, s_i is chosen as the horizontal ellipse center coordinate, i.e., $s_i \equiv c_{x,i}$, because the hole layout and imaging configuration make $c_{x,i}$ a stable proxy for angular ordering.[1]

Within the practical scanning range, the aspect ratio can be locally linearized w.r.t. s_i:

$$\rho_i = a\, s_i + b + \varepsilon_i, \tag{7}$$

where (a, b) are regression coefficients and ε_i summarizes measurement noise.

[1] If the mechanical and optical configuration instead makes $c_{y,i}$ more directly correlated with θ, the same derivation applies by setting $s_i = c_{y,i}$.

3.7.1. Rotation center estimation as linear regression

Stacking N observations gives

$$\mathbf{y} = \mathbf{H}\theta + \boldsymbol{\varepsilon}, \tag{8}$$

with

$$\mathbf{y} = \begin{bmatrix}\rho_1 & \rho_2 & \cdots & \rho_N\end{bmatrix}^\top, \quad \mathbf{H} = \begin{bmatrix} s_1 & 1 \\ s_2 & 1 \\ \vdots & \vdots \\ s_N & 1 \end{bmatrix}, \quad \theta = \begin{bmatrix} a \\ b \end{bmatrix}.$$

The OLS estimate is

$$\hat{\theta}_{\mathrm{OLS}} = (\mathbf{H}^\top \mathbf{H})^{-1} \mathbf{H}^\top \mathbf{y}.$$

The horizontal rotation center is recovered from the zero-crossing:

$$\hat{x}_c = -\frac{\hat{b}}{\hat{a} + \epsilon}, \tag{9}$$

Because $\hat{a}$ appears in the denominator, numerical instability may occur when $\hat{a}$ approaches zero. In implementation, a small positive constant ϵ is added to the denominator to avoid division-by-zero without affecting the estimate under normal conditions. In practice, under the sector-scan geometry, the aspect ratio varies monotonically with angular position, yielding a non-zero slope. Therefore, near-zero slope estimates typically indicate degenerate configurations such as insufficient scan range or corrupted ellipse measurements. To further improve robustness, we adopt robust line fitting (RANSAC followed by trimmed refinement) to suppress corrupted ellipses before final least-squares estimation.

3.7.2. Uncertainty-aware (weighted) regression

Ellipse fitting yields heterogeneous uncertainties across ROIs. Let $\sigma_{\rho,i}^2 = \mathrm{Var}(\rho_i)$ and define $\boldsymbol{\Sigma}_\rho = \mathrm{diag}(\sigma_{\rho,1}^2, \ldots, \sigma_{\rho,N}^2)$. The WLS estimate is

$$\hat{\theta}_{\mathrm{WLS}} = (\mathbf{H}^\top \boldsymbol{\Sigma}_\rho^{-1} \mathbf{H})^{-1} \mathbf{H}^\top \boldsymbol{\Sigma}_\rho^{-1} \mathbf{y}. \tag{10}$$

This covariance-weighted form down-weights ellipses with large uncertainty and improves robustness when ROI quality varies.

3.7.3. Error propagation to rotation center uncertainty

Let $\mathbf{C}_{ab}$ denote the covariance of $(\hat{a}, \hat{b})^\top$ under WLS:

$$\mathbf{C}_{ab} = (\mathbf{H}^\top \boldsymbol{\Sigma}_\rho^{-1} \mathbf{H})^{-1}.$$

Using first-order error propagation on $x_c = -b/a$,

$$\mathrm{Var}(\hat{x}_c) \approx \mathbf{J}_{x_c} \mathbf{C}_{ab} \mathbf{J}_{x_c}^\top, \quad \mathbf{J}_{x_c} = \begin{bmatrix} \frac{b}{a^2} & -\frac{1}{a} \end{bmatrix},$$

which expands to

$$\mathrm{Var}(\hat{x}_c) = \frac{b^2}{a^4}\mathrm{Var}(a) + \frac{1}{a^2}\mathrm{Var}(b) - \frac{2b}{a^3}\mathrm{Cov}(a, b). \tag{11}$$

3.7.4. Observability and sensitivity

The conditioning of the estimation is governed by the information matrix

$$\mathbf{I}_x = \mathbf{H}^\top \boldsymbol{\Sigma}_\rho^{-1} \mathbf{H}.$$

When $\{s_i\}$ are tightly clustered, $\mathbf{I}_x$ becomes ill-conditioned and the slope is weakly observable. To first order, the uncertainty obeys

$$\mathrm{Std}(\hat{x}_c) \propto \frac{\bar{\sigma}_\rho}{\sqrt{N}\,\Delta s}, \tag{12}$$

where Δs is the span of $\{s_i\}$ and $\bar{\sigma}_\rho$ is a representative noise scale.

This motivates a practical ROI policy: prefer spatially distributed ROIs over densely clustered ones. In practice, a sufficiently large span of $\{s_i\}$ is recommended. For example, distributing ROIs across at least 30%-50% of the field of view typically provides stable estimation. From a numerical perspective, using approximately 8-30 well-distributed ROIs is generally sufficient for reliable estimation, while further increasing the number of ROIs yields diminishing returns due to the low dimensionality of the regression problem. Ellipses with large residuals or uncertainties are rejected to further improve robustness. This is consistent with Eq. (16), where increasing the spatial span of the samples contributes more significantly to estimation stability than simply increasing sample density.

3.7.5. Linearized model for angular sampling rate estimation

The angular sampling model (2) implies that the ellipse centers satisfy

$$\theta_i = k(c_{y,i} - y_c) + \eta_i, \tag{13}$$

where η_i summarizes center localization noise and possible non-uniform rotation.

Linearization and higher-order error. The above formulation is derived from a first-order linear approximation of the underlying nonlinear geometric relationship. By expanding the exact model using a Taylor series, the residual error can be expressed as

$$\varepsilon_i \approx \frac{1}{2} f''(\xi_i)\,(k(c_{y,i} - y_c))^2, \tag{14}$$

where ξ_i lies between the linearization point and the true value. This indicates that the approximation error grows quadratically with respect to the scanning angle.

Angular fluctuation modeling. To account for non-uniform angular velocity, we further model the sampling angle as

$$\theta_i = k(c_{y,i} - y_c) + \delta_i + \eta_i, \tag{15}$$

where δ_i represents small perturbations caused by angular velocity fluctuation. These perturbations introduce additional bias in the regression but remain bounded under mild fluctuations.

Linear regression form. The model can be written as a linear regression

$$\theta_i = k\,c_{y,i} + d + \eta_i', \quad d = -k\,y_c,$$

where $\eta_i' = \eta_i + \delta_i + \varepsilon_i$ aggregates noise and model mismatch.

The least-squares estimate of k is

$$\hat{k} = \frac{\sum_i (c_{y,i} - \bar{c}_y)(\theta_i - \bar{\theta})}{\sum_i (c_{y,i} - \bar{c}_y)^2}.$$

Assuming $\eta_i' \sim \mathcal{N}(0, \sigma_\theta^2)$,

$$\mathrm{Var}(\hat{k}) \approx \frac{\sigma_\theta^2}{\sum_i (c_{y,i} - \bar{c}_y)^2}, \tag{16}$$

indicating that reliable estimation requires sufficient vertical distribution (i.e., large span of $c_{y,i}$).

Practical applicability. In typical industrial setups, the effective scanning angular range is limited, under which the higher-order term ε_i remains bounded and is generally small compared to measurement noise.

3.8. Estimation of rotation center via aspect ratio regression

Based on the linearized measurement model introduced in Section 3.7, the horizontal rotation center x_c is estimated from the regression between ellipse aspect ratios and ellipse center positions. This subsection focuses on the practical estimation strategy and robustness considerations.

For the ith detected ellipse, the aspect ratio is defined as

$$\rho_i = \frac{r_{x,i}}{r_{y,i}}, \tag{17}$$

where $r_{x,i}$ and $r_{y,i}$ denote the estimated major and minor axes, respectively. Within the effective angular range of the sector-scan system, the aspect ratio varies approximately linearly with the horizontal ellipse center coordinate:

$$\rho_i = a\,c_{x,i} + b, \tag{18}$$

where $(c_{x,i}, c_{y,i})$ is the center of the ith ellipse, and (a, b) are regression coefficients.

The horizontal coordinate of the rotation center is recovered from the zero-crossing of the fitted model:

$$x_c = -\frac{b}{a}. \tag{19}$$

Based on the linearized measurement model introduced in Section 3.6, the horizontal rotation center x_c is estimated from the regression between ellipse aspect ratios and ellipse center positions. This subsection focuses on the practical estimation strategy and robustness considerations. In typical calibration images, the number of detected ellipses ranges from 8 to 30, resulting in a small-scale regression problem with negligible computational cost.

3.8.1. Baseline least-squares estimation

As a baseline, the coefficients (a, b) can be estimated by ordinary least-squares (OLS) regression using all detected ellipses. This solution is computationally efficient and provides accurate results when all measurements are well-behaved.

However, since the slope a appears in the denominator of (19), the estimation of x_c is highly sensitive to slope bias. Even a small number of severely corrupted ellipses-caused by partial occlusion, specular reflections, or failed contour extraction-can significantly degrade the OLS solution.

3.8.2. RANSAC-based robust line fitting

To suppress gross outliers, a RANSAC-based line fitting strategy is employed. At each RANSAC iteration, a minimal subset of ellipse measurements is randomly sampled to estimate a candidate line model. The residual of the ith measurement is evaluated as

$$\epsilon_i = \left|\rho_i - (a\,c_{x,i} + b)\right|. \tag{20}$$

Measurements whose residuals fall below a predefined threshold are classified as inliers. After a fixed number of iterations, the model supported by the largest inlier set is selected as the initial estimate. This step ensures that the estimated slope reflects the dominant geometric trend rather than being biased by a few erroneous ellipses.

RANSAC is adopted due to its robustness to gross outliers arising from ellipse fitting failures, incomplete contours, or spurious detections under degraded imaging conditions. In this application, the number of observations is small and the regression model is low-dimensional, making RANSAC computationally efficient and sufficiently robust. Moreover, the extracted ellipse parameters are largely consistent, resulting in a high inlier ratio (typically above 95%), under which the randomness of RANSAC is reduced and the estimation becomes more stable. Since the dominant disturbances are sparse but significant outliers rather than dense noise, RANSAC provides an effective solution, and more complex robust estimators are unlikely to offer substantial additional benefits in this setting.

3.8.3. Iterative residual-Based least square refinement (ILS)

While ordinary least squares (OLS) provides an efficient initial estimate, it is sensitive to outliers and moderately corrupted measurements. To improve robustness without introducing random sampling, an iterative residual-based refinement strategy is adopted.

Starting from the OLS solution, residuals are computed for all measurements. The residual distribution is characterized by its mean μ_ϵ and standard deviation σ_ϵ. Measurements satisfying

$$\epsilon_i \le \mu_\epsilon + \lambda\sigma_\epsilon, \tag{21}$$

where $\lambda \in [2, 3]$, are retained as reliable inliers, and the regression parameters are re-estimated using least squares.

This trimming-and-refitting procedure can be interpreted as a reweighted least squares process, where measurements with large residuals are progressively suppressed. The iteration continues until convergence, defined as

$$\|\Delta \mathbf{w}\| < \varepsilon, \tag{22}$$

where $\mathbf{w} = (a, b)$ denotes the regression parameters and ε is a small threshold (e.g., 10^{-3}).

In practice, due to the low dimensionality of the problem and the high inlier ratio, the algorithm typically converges within a few iterations (2–3 iterations). A maximum iteration number is imposed as a safeguard against rare unstable cases.

This iterative refinement yields a stable and statistically consistent estimate of the regression parameters (a, b) under moderate noise and partial outlier contamination.

The monotonic suppression of large residuals further promotes stable convergence behavior.

3.8.4. Reliability and observability assessment

The reliability of the estimated rotation center is evaluated using the coefficient of determination R^2 of the final regression. A high R^2 indicates sufficient angular diversity among the detected ellipses and validity of the linear approximation in (18).

When the total scanned angle is too small, ellipses degenerate toward circles and the variation of ρ_i becomes weak. In such cases, the regression becomes ill-conditioned and the estimation of x_c is unreliable. This behavior provides a practical observability criterion for assessing calibration quality.

3.9. Sector-to-cartesian unwarping

Given the estimated parameters (x_c, y_c, k), we perform inverse mapping to generate a rectified image without holes. For a target rectified pixel (u, v), we define

$$r = u, \qquad \theta = v\,\Delta\theta,$$

and map it back to the distorted image coordinate

$$x = x_c + r, \qquad y = y_c + \theta/k.$$

Intensity values are obtained by bilinear interpolation. The unwarped image restores metric consistency and converts distorted ellipses back to circular holes.

3.10. Extension to 3D height map correction

For laser profilometry, each observed height value $Z(x, y)$ corresponds to a 3D point whose in-plane coordinates are governed by the sector geometry. After correction,

$$X = r\cos\theta, \tag{23}$$

$$Y = r\sin\theta, \tag{24}$$

$$Z = Z(x, y), \tag{25}$$

yielding a geometrically consistent point cloud in which distortions caused by sector sampling and mounting misalignment are suppressed. It should be noted that this transformation addresses geometric distortions arising from scanning geometry, while system-level optical factors such as laser plane calibration and focal length variations are not explicitly modeled.

4. Experiments

This section evaluates the proposed geometric calibration and unwarping method on a real rotating line-scan 2D/3D imaging system. We report (1) ellipse detection and fitting accuracy, (2) estimation of global geometric parameters, (3) 2D image unwarping quality, (4) correction performance on 3D height maps, and (5) robustness analyses via controlled variations of ROI selection and regression strategies. All experiments are conducted on an industrial laser line-scan measurement system mounted above a motorized rotary stage.

4.1. Experimental setup

All experiments are conducted on a rotating laser line-scan measurement system, as illustrated in Fig. 2. Unlike conventional setups that employ separate sensors for 2D and 3D acquisition, our system uses a single industrial 3D laser profiler to simultaneously acquire both 2D intensity images and 3D height profiles.

Hardware configuration. The core sensing device is a laser triangulation profiler (LPF2-050, OPT Machine Vision), mounted above a programmable precision rotary stage. The profiler employs a blue laser source with a wavelength of 405 nm, providing stable stripe contrast on metallic and reflective surfaces. The nominal working distance is 500 mm, and the Z-axis measurement range is approximately 430 mm.

The profiler operates in line-scan mode and can be regarded as a 3D line-scan camera: each acquired scan line yields a one-dimensional height profile via laser triangulation, while the corresponding reflected intensity values form a 2D line-scan image. As a result, both 2D intensity images and 3D height maps are generated from the same raw measurements and share an identical sector-scan imaging geometry.

Each scan line contains 3200 sampling points along the lateral direction, with a spatial sampling interval ranging from 58 μm to 119 μm depending on the working distance. According to manufacturer specifications, the repeatability is approximately 30 μm along the X-axis and 5 μm along the Z-axis, with a linearity of $\pm 0.02\%$ of the full-scale range. These characteristics provide sufficient measurement fidelity for evaluating geometric calibration and unwarping accuracy.

Rotating sector-scan configuration. During acquisition, the laser profiler remains stationary while the calibration target is mounted on the rotary stage and rotates at a constant angular velocity. This configuration produces a sector-scan (polar) sampling geometry, where successive scan lines correspond to different angular positions of the rotating stage. The profile acquisition rate is configured between 3000 and 18,000 profiles per second depending on the rotation speed, ensuring dense angular sampling while avoiding motion-induced artifacts.

Calibration targets and data representation. Three circular hole-pattern calibration plates made of different materials are used in the experiments, each with distinct hole layouts and surface properties. All calibration targets are mounted on the same rotary stage and scanned under identical acquisition settings.

A typical raw sector-scan image acquired by the laser profiler is shown in Fig. 3. Due to polar sampling induced by rotational motion, circular holes on the calibration plates are distorted into ellipses whose aspect ratios and center positions vary systematically across the field of view. These elliptical distortions encode the underlying sector-scan geometry and are largely insensitive to the material properties of the calibration targets.

The geometric parameters estimated from the ellipse analysis are subsequently used to construct a unified polar-to-Cartesian unwarping transformation. This transformation is applied consistently to both 2D line-scan intensity images and 3D laser-based height maps, enabling joint geometric correction within a single calibration framework.

4.2. Evaluation metrics

To quantitatively evaluate the effectiveness of the proposed calibration and unwarping method, we adopt a set of geometry-driven metrics that jointly assess local shape recovery, global geometric consistency, and structural regularity. All metrics are computed automatically from corrected images without manual annotation.

The evaluation focuses on three complementary aspects: (i) circularity of recovered holes, (ii) linearity of grid structures, and (iii) consistency of spatial spacing.

(a) Metallic calibration board

(b) Ceramic calibration board

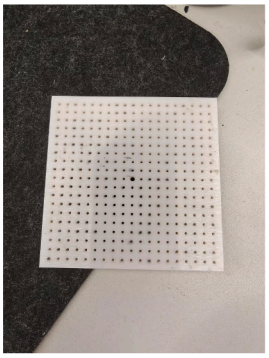

(c) Ceramic calibration board

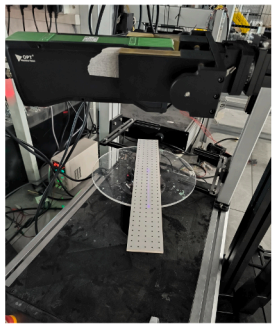

(d) Rotating line-scan experimental setup

Fig. 2. Calibration targets and experimental setup. (a)–(c) Circular hole-pattern calibration plates made of different materials, including metallic and ceramic substrates, with varying hole layouts. Despite differences in material properties and geometric configurations, all targets produce consistent estimates of the rotation center and angular sampling parameters. (d) Real experimental setup consisting of a rotating stage and a laser line-scan profiler operating under sector-scan geometry.

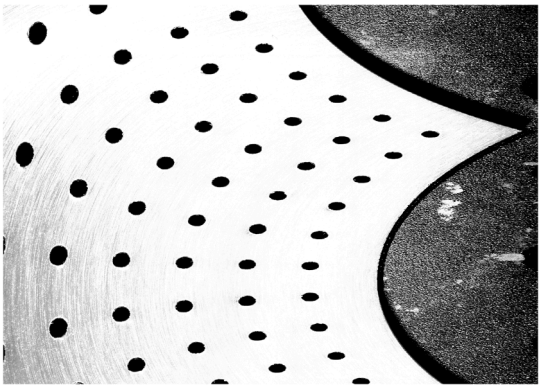

Fig. 3. Raw line-scan image before calibration. Circular holes appear as ellipses due to sector-scan distortion.

4.2.1. Circularity (roundness)

For each detected hole, an equivalent ellipse is estimated from second-order moments, yielding major and minor radii r_x and r_y. The roundness is defined as

$$\text{Roundness}_i = \frac{\min(r_x, r_y)}{\max(r_x, r_y)}. \tag{26}$$

The overall circularity score is the mean roundness:

$$\overline{\text{Roundness}} = \frac{1}{N}\sum_{i=1}^{N} \text{Roundness}_i. \tag{27}$$

4.2.2. Linearity of grid structures

Let $\{\mathbf{p}_i\}$ denote detected hole centers. A dominant grid direction is estimated using robust line fitting, and points are rotated accordingly. After grouping points into rows, the RMS deviation for row j is

$$\text{RMS}_j = \sqrt{\frac{1}{M_j}\sum_{k=1}^{M_j} d_{jk}^2}, \tag{28}$$

where d_{jk} is the perpendicular distance to the fitted line. The global linearity is

$$\text{Linearity} = \frac{1}{J}\sum_{j=1}^{J} \text{RMS}_j. \tag{29}$$

Lower values indicate less residual distortion.

4.2.3. Spacing consistency

Neighboring center distances $\{s_i\}$ are computed along the dominant grid direction. The coefficient of variation (CV) is used:

$$\text{CV}_{\text{spacing}} = \frac{\sigma_s}{\mu_s}, \tag{30}$$

where μ_s and σ_s are the mean and standard deviation.

4.2.4. Composite evaluation score

A composite score aggregates the normalized metrics:

$$\text{Score} = w_r S_{\text{round}} + w_l S_{\text{lin}} + w_c S_{\text{cons}}, \tag{31}$$

with $w_r = 0.40$, $w_l = 0.35$, and $w_c = 0.25$.

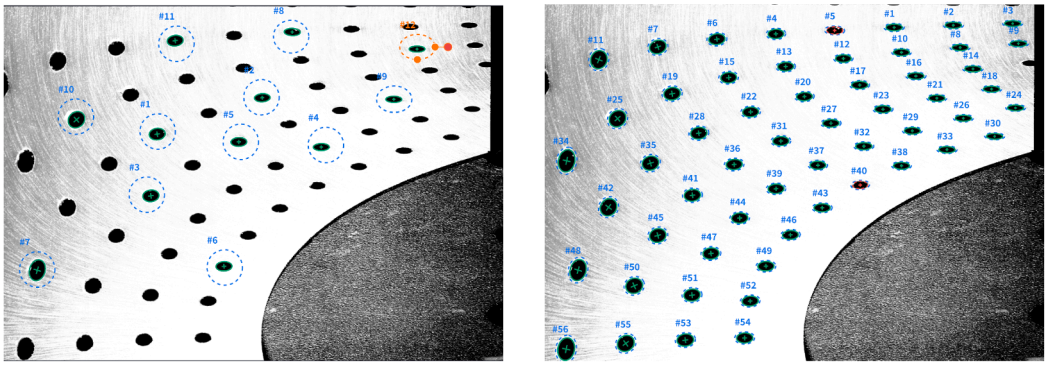

(a) Manual ROI selection (b) Automatic ROI detection

Fig. 4. Examples of manual and automatic ellipse detection results.

4.3. Ellipse detection and fitting accuracy

We extract 5–20 ROIs across the field of view manually, and alternatively use an automatic ellipse detection method to generate ROIs for each ellipse. Fig. 4 shows examples.

Ellipse fitting accuracy is quantified by the RMS algebraic distance:

$$\varepsilon = \sqrt{\frac{1}{N}\sum_{j=1}^{N}\left(Ax_j^2 + Bx_jy_j + Cy_j^2 + Dx_j + Ey_j + F\right)^2}. \tag{32}$$

Across all ROIs, the average fitting error is

$$\varepsilon_{\text{avg}} = 0.42 \text{ pixels}. \tag{33}$$

4.4. Estimation of rotation center and angular mapping

Using fitted ellipses, aspect ratios $\rho_i = r_{x,i}/r_{y,i}$ are regressed against horizontal centers $c_{x,i}$. The estimated rotation center is

$$x_c = -516.76, \tag{34}$$

with coefficient of determination

$$R^2 = 0.998. \tag{35}$$

Estimating the angular sampling rate k using the linearized angular model in Section 3.7 (Eqs. (13)—((14)) yields

$$k = 0.00402 \text{ rad/pixel}, \tag{36}$$

with residual angular error below $0.12°$ across all calibration holes.

A visualization of regression results is provided in Fig. 5.

4.5. 2D unwarping of the sector-scan image

Using the recovered parameters (x_c, y_c, k), the entire image is unwarped to a rectilinear grid. Fig. 6 compares raw and corrected images.

Circularity is additionally reported as

$$\epsilon = \frac{|r_x - r_y|}{r_x}. \tag{37}$$

Before correction: $\epsilon_{\text{before}} = 0.21 \pm 0.08$. After correction: $\epsilon_{\text{after}} = 0.02 \pm 0.01$.

4.6. 3D height map correction

The same transformation is applied to 3D line-scan data. Fig. 7 shows the results of the corrected 3D surface of the calibration board.

To assess the effect of geometric correction on 3D reconstruction, we analyze the geometric consistency of the reconstructed height maps before and after unwarping. After correction, the reconstructed surfaces exhibit significantly reduced residual geometric distortion and improved spatial regularity, indicating that the proposed unwarping transformation effectively reduces geometric distortions related to rotational scanning in 3D line-scan data.

Table 1
Effect of ROI count on calibration stability.

ROI Count	Mean x_c (px)	Std. Dev. (px)	Total Score
5	−518.3	2.1	78.5
8	−517.6	1.2	83.9
10	−516.9	0.6	86.8
15	−516.7	0.4	87.5
20	−516.8	0.3	87.9
Auto	−516.8	0.3	88.1

4.7. Statistical analysis

We analyze two key factors affecting calibration stability: ROI selection and regression strategy.

4.7.1. Effect of ROI count on rotation center estimation

To evaluate the influence of the number of detected ellipses, we vary the number of ROIs used for regression while keeping their spatial distribution approximately uniform across the field of view (Fig. 8). For each configuration, a subset of $N \in \{5, 8, 10, 15, 20\}$ ellipses is randomly selected from the detected set. The "Auto" configuration corresponds to automatic ROI detection followed by robust regression with iterative residual-based least squares refinement (ILS). The procedure is repeated 50 times.

Table 1 reports the mean estimated rotation center and the corresponding standard deviation for different ROI counts. The estimation results under varying numbers of selected ellipses are summarized for comparison.

Fig. 9 shows representative ROI selection patterns at 50 rpm together with their corresponding evaluation or unwarping results.

4.7.2. Comparison of regression strategies

We compare three regression strategies: ordinary least squares (OLS), RANSAC-based regression, and iterative residual-based least squares refinement (ILS). Experiments are conducted at rotation speeds from 20 to 300 rpm. For each speed, the same set of detected ellipses is used, and only the regression strategy is varied.

Table 2 reports the evaluation scores obtained under different rotation speeds and regression strategies. In addition, Table 3 summarizes the estimated rotation center xc, coefficient of determination R2, and the corresponding standard deviation for each method.

Fig. 5. Regression of ellipse aspect ratios and angular mapping.

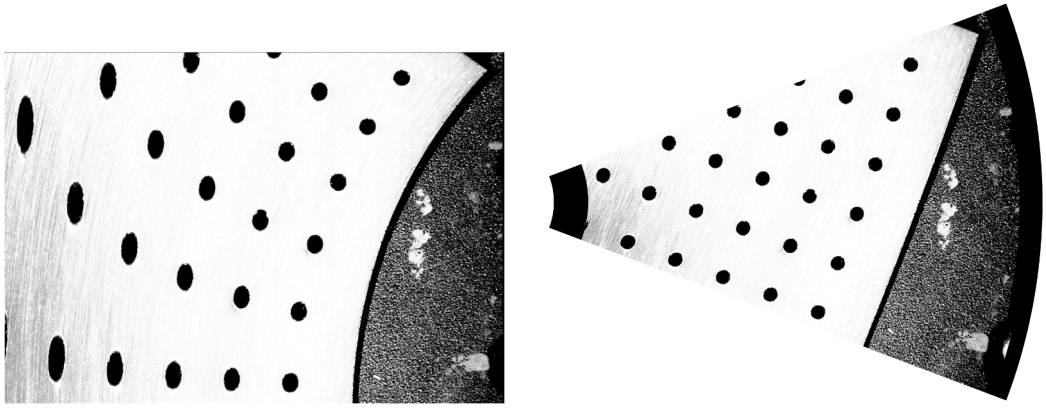

(a) Before unwarping (b) After unwarping

Fig. 6. 2D unwarping results of the sector-scan image. Circular holes are restored after correction.

Table 2
Comparison of regression strategies under different rotation speeds.

RPM	Method	Total Score	Linearity	Roundness
20	OLS	73.7	55.0	78.0
	RANSAC	87.0	85.7	85.0
	ILS	87.7	85.7	85.0
50	OLS	75.5	53.5	83.5
	RANSAC	75.0	52.5	83.5
	ILS	75.0	53.0	83.5
100	OLS	59.5	10.0	86.5
	RANSAC	60.0	12.0	86.0
	ILS	59.5	11.5	86.0
300	OLS	94.0	96.0	95.0
	RANSAC	94.0	96.0	95.0
	ILS	89.7	80.3	95.0

4.8. Robustness analysis under degraded imaging conditions

To further evaluate the validity of the linearization assumption adopted in the core derivations, we investigate the robustness of the proposed method under several degraded imaging conditions. These conditions simulate practical factors that may introduce systematic errors in ellipse estimation and affect the linearized geometric model, including partial occlusion, image noise, and defocus blur.

Specifically, six representative scenarios are considered: original images, two types of partial occlusion (dark blob and mixed blob), two types of image noise (salt-and-pepper and speckle noise), and defocus blur. For each scenario, the ellipse extraction and geometric unwarping procedures are applied using the same calibration pipeline.

Parameter settings of degradation. All degraded scenarios are generated using the *high* severity level to simulate challenging industrial conditions.

Specifically, for noise and blur: Gaussian blur is applied with kernel size 15 and standard deviation $\sigma = 5.0$; salt-and-pepper noise is added with corruption probability 0.12; speckle noise is modeled as multiplicative noise with $\sigma = 0.30$.

For occlusion: Gaussian blob-based perturbations are used, where 25–35 blobs are randomly generated, with spatial scale (standard deviation) ranging from 20 to 80 pixels, and intensity up to 0.9, resulting in significant partial coverage of the ellipse boundaries.

These parameter settings correspond to moderate-to-severe degradation levels, therefore providing a stress-test of the proposed method under adverse imaging conditions. The results are shown in Fig. 10.

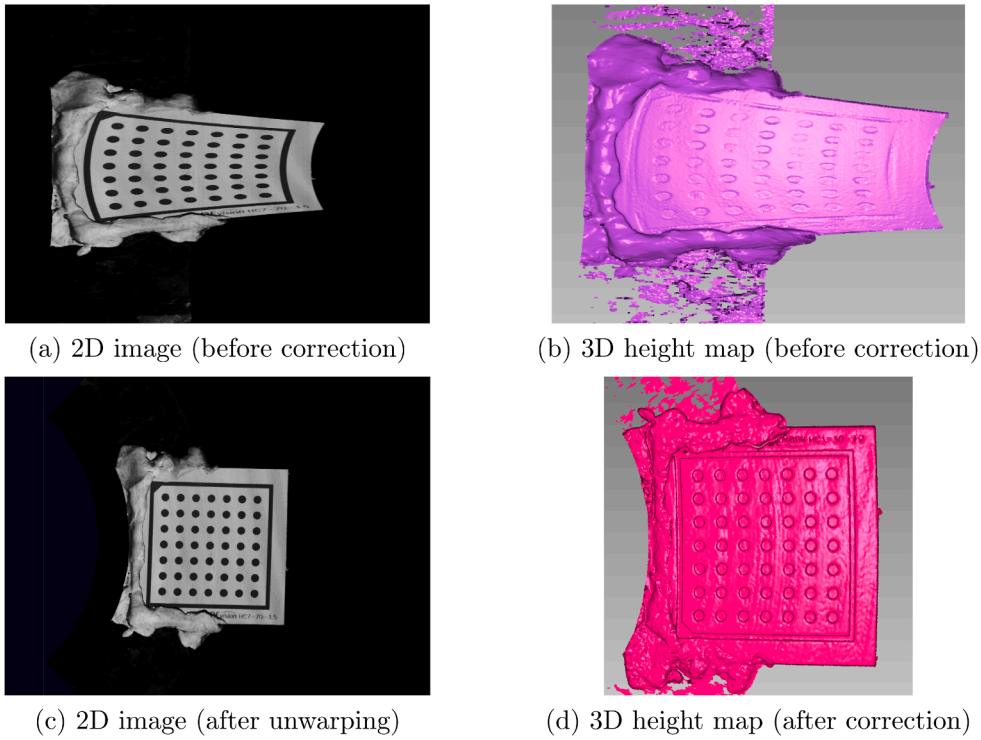

(a) 2D image (before correction) (b) 3D height map (before correction)

(c) 2D image (after unwarping) (d) 3D height map (after correction)

Fig. 7. 3D height-map correction with corresponding 2D images. Left: 2D line-scan images. Right: reconstructed 3D height maps.

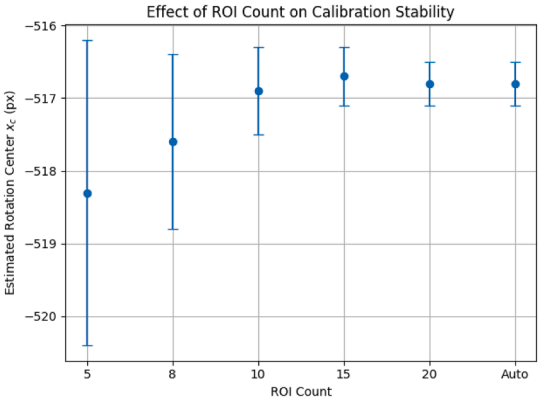

Fig. 8. Effect of ROI count on the stability of rotation center estimation. Error bars indicate ±1 standard deviation over repeated trials.

4.8.1. *Effect of partial occlusion*

Partial occlusion is simulated by introducing dark blob and mixed blob disturbances that partially obscure the circular-hole patterns. These scenarios reduce the visible ellipse boundary and may affect ellipse fitting accuracy. As shown in Fig. 10, the proposed method remains stable despite partial pattern occlusion, indicating that the linearization model is robust to incomplete geometric observations.

4.8.2. *Effect of image noise*

To evaluate noise sensitivity, salt-and-pepper noise and speckle noise are added to the original images. These noise types represent impulsive noise and multiplicative noise commonly observed in industrial imaging systems. The results demonstrate that the ellipse extraction and geometric correction remain stable under moderate noise levels, suggesting that the linearized model is resilient to measurement noise.

Table 3
Regression statistics for rotation center estimation.

Method	x_c (px)	R^2	Std. Dev. (px)
OLS	−503.1	0.962	3.8
RANSAC	−515.4	0.991	1.4
ILS	−516.8	0.998	0.5

4.8.3. *Effect of defocus blur*

Defocus blur is introduced using Gaussian blur to simulate out-of-focus imaging conditions. This degradation primarily affects edge sharpness and ellipse detection accuracy. As shown in Fig. 10, the proposed method still produces consistent calibration and unwarping results, indicating that the linearization assumption remains valid under moderate defocus conditions.

4.9. *Summary*

The experimental results confirm that the proposed method accurately estimates the rotation center and angular sampling, restores circularity of calibration holes to subpixel accuracy, and substantially improves 3D reconstruction consistency. Further interpretation and practical guidelines are provided in Section 5.

5. Discussion

The experimental results demonstrate that elliptical distortions of circular-hole patterns provide strong geometric constraints for calibrating rotating line-scan imaging systems. We discuss observability conditions, robustness to ROI selection and fitting noise, applicability to 3D profilometry, and practical limitations and extensions.

5.1. *Observability and sensitivity to angular coverage*

A key requirement for stable parameter estimation is sufficient angular variation among detected ellipses. When the total scanned angle

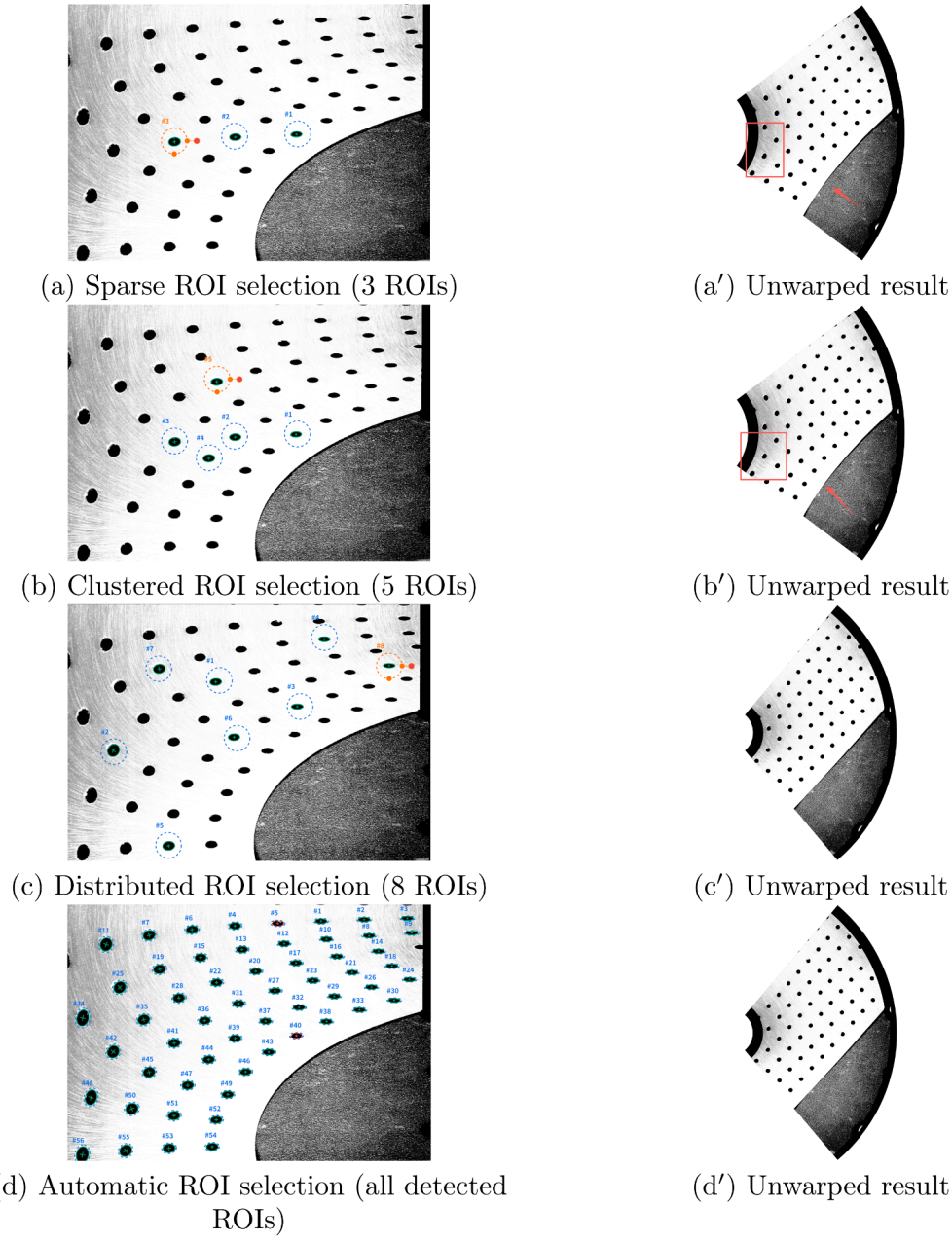

Fig. 9. Representative ROI selection patterns at 50 rpm and corresponding results.

exceeds approximately 10°, ellipse aspect ratios vary significantly across the field of view and lead to stable regression results ($R^2 > 0.99$ in most experiments). When the angular range becomes too small, ellipses approach circular shapes and the aspect-ratio model becomes weakly informative. In such cases, rotation center estimation becomes ill-conditioned and the recovered parameters exhibit higher variance. In practice, the calibration plate should span at least several degrees of rotation during acquisition to ensure reliable observability.

5.2. *Influence of ROI distribution and statistical consistency*

The results in Section 4.7.1 indicate that calibration stability depends on both ROI count and spatial distribution. Using a small number of ellipses can already yield a reasonable estimate of the rotation center, while increasing ROI count reduces variance. This behavior implies that the calibration framework does not require highly precise measurements for each ellipse; instead, it benefits from aggregating multiple weak observations distributed across the field of view.

From a geometric perspective, ellipses located at different radial and angular positions provide complementary constraints on the rotation center. Sparse or locally clustered ROI selections may underconstrain certain deformation components, whereas distributed ROIs improve observability by sampling a wider range of rotational distortions. The improved stability with larger ROI sets also supports a statistical-consistency view: individual ellipse fits may be noisy or partially corrupted, but their errors remain approximately unbiased, so aggregation suppresses random errors.

5.3. *Noise robustness and regression strategy*

The comparison in Section 4.7.2 highlights the impact of outliers and fitting noise. Table 2 compares different regression strategies under varying rotation speeds using image-based geometric metrics, while

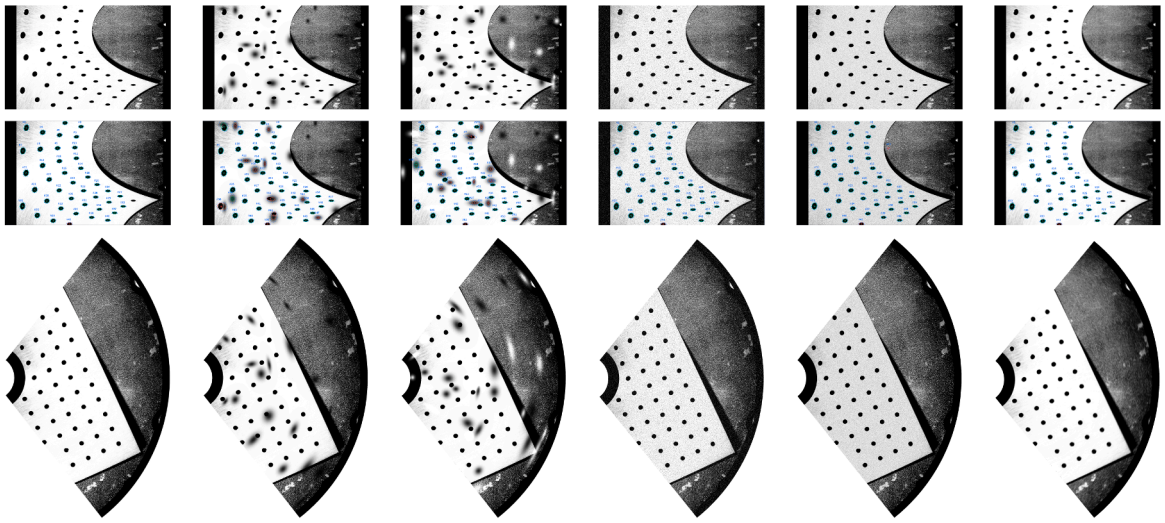

Fig. 10. Robustness evaluation under degraded imaging conditions. Top row: input images under different degradations. Middle row: ellipse extraction results. Bottom row: corrected images after geometric unwarping. From left to right: original, dark blob occlusion, mixed blob occlusion, salt-and-pepper noise, speckle noise, and Gaussian blur. The results demonstrate that the proposed method remains stable under various imaging degradations.

Table 3 focuses on the statistical properties of the estimated rotation center. Several important observations can be drawn. First, ordinary least squares (OLS) regression exhibits noticeable bias and instability, as reflected by a relatively low R^2 value and a large standard deviation of the estimated rotation center. This behavior indicates that OLS is highly sensitive to corrupted or poorly fitted ellipses, which are unavoidable in practical sector-scan imaging. Second, RANSAC-based regression significantly improves robustness by suppressing gross outliers, leading to higher R^2 values and reduced variance. However, the remaining estimation variance suggests that random sampling alone does not fully exploit the statistical consistency among inlier ellipses. Finally, the proposed iterative residual-based least squares refinement (ILS) achieves the most stable and accurate results across all evaluated conditions. As shown in Table 3, ILS yields the highest R^2 value (0.998) and the lowest standard deviation (0.5 px), indicating both strong linear consistency and superior estimation precision. These results confirm that combining outlier rejection with iterative refinement is essential for reliable rotation center estimation in the presence of measurement noise and partial ellipse corruption.

In summary, OLS is sensitive to corrupted ellipse measurements because individual fitting errors directly propagate into the regression model. RANSAC improves robustness by suppressing gross outliers through random sampling, but may introduce additional variance due to sampling randomness. ILS mitigates this trade-off by first rejecting outliers and then refining the model using statistically consistent samples, leading to improved stability across rotation speeds.

5.4. Applicability to 3D laser profilometry

The proposed geometric model is directly applicable to 3D line-scan profilometry, requiring only a modification of the lateral coordinate mapping to the real-world size under polar geometry. When applied to 3D height profiles acquired by the laser profiler, the same unwarping transformation reduces rotational sampling artifacts and improves geometric consistency of the reconstructed surfaces. It should be noted that the proposed correction primarily addresses distortions caused by scanning geometry. Other factors affecting measurement accuracy, such as laser plane calibration and focal length variations, are not explicitly considered in the current model. Therefore, the method improves geometric consistency but does not fully compensate for system-level optical errors. These results indicate that the proposed method can be extended to 3D line-scan data within a unified geometric framework.

5.5. Limitations

Despite its practical effectiveness, the proposed method has several limitations. First, the current formulation assumes the rotation axis is perpendicular to the image plane; axis tilt or wobble would require additional parameters to model perspective-induced deformation. Second, very small scanned angles reduce observability of both the rotation center x_c and the polar scaling factor k as ellipses become nearly circular. Third, strong lens distortion may interact with polar deformation and bias ellipse fitting; undistortion should be applied when significant distortion is present. Fourth, the current derivation assumes that the acquired scan line (i.e., the laser/camera line-of-sight in the image domain) passes through the disk center. If the scan line is laterally offset from the disk center, an additional offset parameter (and corresponding constraints) is required; otherwise, the estimated rotation center may be biased. Finally, non-planarity or warping of the calibration plate can introduce systematic deviations in estimated ellipse centers.

5.6. Future extensions

Future work includes extending the model to account for axis tilt and eccentricity, designing calibration targets optimized for observability under limited angular motion, incorporating learning-based ellipse detection/fitting for low-SNR scenarios, and developing online parameter updating to compensate for thermal drift or dynamic misalignment.

6. Conclusion

This paper presented a complete geometric calibration and unwarping framework for rotating line-scan 2D and 3D imaging systems based on elliptical distortions of circular-hole calibration patterns. By jointly exploiting ellipse centers, aspect ratios, and orientations under sector-scan geometry, the proposed method estimates the rotation center and angular sampling rate in a fully image-driven manner, without requiring mechanical measurements, encoders, or external metrology instruments.

The method relies on a simple circular-hole calibration plate and a unified sector-to-Cartesian unwarping model, which is consistently applied to both 2D intensity images and 3D line-scan data. All ellipse detection, parameter estimation, and regression steps can be performed automatically, and robustness is achieved through statistical aggrega-

tion of multiple weak geometric observations rather than highly precise local feature extraction.

Experiments on real industrial systems demonstrate that the proposed framework effectively corrects sector-scan distortions, restores the geometric regularity of circular features in 2D images, and significantly reduces rotational sampling artifacts in reconstructed 3D surfaces. These results confirm that the method is applicable to both 2D and 3D rotating line-scan imaging within a single geometric calibration framework.

Overall, the proposed approach provides a low-cost, encoder-free, and deployable solution for calibrating rotating line-scan cameras and laser profilometers, with strong potential for industrial inspection, metrology, and automated manufacturing applications.

CRediT authorship contribution statement

Ling Cao: Writing – review & editing, Project administration, Funding acquisition, Data curation, Conceptualization; **Wenxin Zhang:** Writing – original draft, Formal analysis, Data curation; **Daquan Feng:** Supervision, Project administration, Funding acquisition; **Wei Pan:** Writing – review & editing, Writing – original draft, Validation, Software, Project administration, Methodology, Formal analysis, Data curation, Conceptualization.

Data availability

The data and code that support the findings of this study are available from the corresponding author upon reasonable request.

Declaration of competing interests

The authors declare the following financial interests/personal relationships which may be considered as potential competing interests:

Wei Pan reports financial support was provided by OPT Machine Vision. Wei Pan reports a relationship with OPT Machine Vision that includes: employment. Wei Pan has patent # CN121724877A pending to licensee. The authors declare that they have no known competing financial interests or personal relationships that could have influenced the work reported in this paper. The research was conducted as part of the authors' institutional activities, and no external commercial interests have influenced the results. If there are other authors, they declare that they have no known competing financial interests or personal relationships that could have appeared to influence the work reported in this paper.

Acknowledgments

This work was funded by OPT Machine Vision under the Dongguan Key Research and Development Program (No. 20241200300122) and the Guangdong Provincial Key Research and Development Program (No. 2025B0101120001).

References

[1] Pan W, Jiang B-f, Tang W-m, Wu F-p, Li S-p. Gap measurement method based on projection lines and convex analysis of 3D points cloud. Meas Sci Technol 2024;35(10):105024.
[2] Cao L, Zhou R, Wang X, Pan W. Precision 3d volume measurement of transparent adhesives via spectrally optimized line laser scanning and enhanced centroid extraction. Meas Sci Technol 2025;36(11):115206.
[3] Luna CA, Vazquez JF, Mazo M, Lazaro JL. Calibration of line-scan cameras. IEEE Trans Instrum Meas 2010;59(8):2185–90. https://doi.org/10.1109/TIM.2009.2031344
[4] Niu M, Song K, Wen X, Zhang D, Yan Y. The line scan camera calibration based on space rings group. IEEE Access 2018;6:1–13. https://doi.org/10.1109/ACCESS.2018.2817629
[5] Hui B, Wen G, Zhang P, Li D. A novel line scan camera calibration technique with an auxiliary frame camera. IEEE Trans Instrum Meas 2013;62(9):2567–75. https://doi.org/10.1109/TIM.2013.2256815
[6] Li P, Dou P, Su Z, Lu L, Pan W. Deep transformer-enhanced dynamic structured light for three-dimensional moving object imaging. Opt Express 2025;33(25):52084–104.
[7] Lu L, Bu C, Su Z, Guan B, Yu Q, Pan W, et al. Generative deep-learning-embedded asynchronous structured light for three-dimensional imaging. Adv Photon 2024;6(4):046004.
[8] Petty RS, Robinson M, Evans JPO. 3D measurement using rotating line-scan sensors. Meas Sci Technol 1998;9(3):339–46. https://doi.org/10.1088/0957-0233/9/3/005
[9] Ha V-T, Do V-P, Lee B-R. Calibration method of a three-dimensional scanner based on a line laser projector and a camera with one-axis rotating mechanism. Opt Eng 2024;63(3):033101. https://doi.org/10.1117/1.OE.63.3.033101
[10] Tsai T-H, Fan K-C. Calibration and analysis of eccentric error of the laser rotary-scanning measurement system. Measurement 2012;45(1):47–53. https://doi.org/10.1016/j.measurement.2011.10.005
[11] Dudás L, Gajdátsy G, Sinkó J, Erdélyi M, Szabó G. Correction of error motion in a line-scanning tomographic optical microscope. Appl Opt 2012;51(26):6319–24. https://doi.org/10.1364/AO.51.006319
[12] Lee MH, Kim JH, Park SB. Analysis of a scan conversion algorithm for a real-time sector scanner. IEEE Trans Med Imaging 1986;5(2):96–105. https://doi.org/10.1109/TMI.1986.4307753
[13] Xu B, Shimizu Y, Ito S, Gao W. Pitch deviation measurement of an involute spur gear by a rotary profiling system. Precis Eng 2015;39:152–60. https://doi.org/10.1016/j.precisioneng.2014.08.003
[14] Morales J, Martínez JL, Mandow A. Boresight calibration of construction misalignments for 3d scanners built with a 2D laser rangefinder rotating on its optical center. Sensors 2014;14(11):20025–40. https://doi.org/10.3390/s141120025
[15] Li X, Zhang W, Song G. Calibration method for line-structured light three-dimensional measurements based on a single circular target. Photonics 2022;9(4):218. https://doi.org/10.3390/photonics9040218
[16] Dai G, Zhang Q, Xu X, Zhao B. A calibration method of line-structured light system for measuring outer circle dimension during machining. Results Eng 2024;23:102525. https://doi.org/10.1016/j.rineng.2024.102525
[17] Sergiyenko O, editor. Optoelectronic devices in robotic systems. Cham: Springer; 2022. ISBN 978-3-031-09791-1. https://doi.org/10.1007/978-3-031-09791-1
[18] Sergiyenko O, Alaniz-Plata R, Flores-Fuentes W, Rodríguez-Quiñonez J, Miranda-Vega J, Sepulveda-Valdez C, et al. Multi-view 3d data fusion and patching to reduce shannon entropy in robotic vision. Opt Lasers Eng 2024;177:108132.
[19] Sergiyenko OY, Tyrsa VV. 3D optical machine vision sensors with intelligent data management for robotic swarm navigation improvement. IEEE Sens J 2021;21(10):11262–74. https://doi.org/10.1109/JSEN.2020.3007856
[20] Sergiyenko OY, Ivanov MV, Tyrsa VV, Kartashov VM, Rivas-López M, Hernández-Balbuena D, et al. Data transferring model determination in robotic group. Rob Auton Syst 2016;83:251–60.
[21] Sun B, Zhu J, Yang L, Yang S, Niu Z. Calibration of line-scan cameras for precision measurement. Appl Opt 2016;55(25):6836–43. https://doi.org/10.1364/AO.55.006836
[22] Usamentiaga R. Static calibration for line-scan cameras based on a novel calibration target. IEEE Trans Instrum Meas 2022;71:1–12. https://doi.org/10.1109/TIM.2022.3190039
[23] Lian D, Huang J, Yang R, Gao S, Zheng Y, Liu Y, et al. A calibration method for telecentric line-scan cameras with an enhanced dynamic imaging model. Measurement 2025;241:115743. https://doi.org/10.1016/j.measurement.2024.115743
[24] Berkhoff AP, Huisman HJ, Thijssen JM, Jacobs EMGP, Homan RJF. Fast scan conversion algorithms for displaying ultrasound sector images. Ultrason Imaging 1994;16(2):87–108. https://doi.org/10.1177/016173469401600203
[25] Lee J, Kim H, Park S. Development of a wide area 3d scanning system with a rotating line laser. Sensors 2021;21(12):3939.
[26] Cuesta E, Giganto S, Álvarez BJ, Barreiro J, Martínez-Pellitero S, Meana VM. Laser line scanner aptitude for the measurement of selective laser melting parts. Opt Lasers Eng 2021;138:106406. https://doi.org/10.1016/j.optlaseng.2020.106406
[27] Zheng J, Chen G, Wang L, Sheng X, Liu X, Gao T, et al. Alignment method for rotary stage axis and optical axis in the polar coordinate direct laser writing system. Opt Eng 2022;61(3):034104. https://doi.org/10.1117/1.OE.61.3.034104
[28] Lyu LF, Zhu WD, Will DT, Yuan K. A novel misalignment angle correction method for vibration measurement of a rotating structure using an image-based tracking continuously scanning laser doppler vibrometer. Opt Laser Technol 2025;190:113155. https://doi.org/10.1016/j.optlastec.2025.113155
[29] Zhao C, Yang L, Xu G. Camera calibration method based on ellipse eccentricity compensation. Meas Sci Technol 2024;35(12):125002.
[30] Song C, Lee D, Lim J, Kim A. Camera calibration via circular patterns: a comprehensive framework with measurement uncertainty and unbiased projection model. arXiv preprint arXiv:250616842 2025.
[31] Fitzgibbon A, Pilu M, Fisher RB. Direct least squares fitting of ellipses. IEEE Trans Pattern Anal Mach Intell 1999;21(5):476–80. https://doi.org/10.1109/34.765658
[32] Martínez-Otzeta JM, Rodriguez I, Lazkano E, Sierra B. Ransac for robotic applications: a survey. Sensors 2022;22(2):475.
[33] Zhang G, Wang Y, Chen L. Ransac-based ellipse fitting with adaptive outlier rejection. Comput Vision Image Understanding 2024;219:103658.
[34] Chen XD, Zhang L, Zhou H. Improving ellipse fitting via multi-scale smoothing and key-point detection. Pattern Recognit 2024;145:110432.

[35] Zhou H, Chen X, Zhang J. A high-precision ellipse detection method based on deep learning. Pattern Recognit 2024;158:108456.
[36] Genta G, Minetola P, Barbato G. Calibration procedure for a laser triangulation scanner with uncertainty evaluation. Opt Lasers Eng 2016;86:11–19. https://doi.org/10.1016/j.optlaseng.2016.05.005
[37] Fei L, Tong X, Liu Q. Calibration and uncertainty estimation of non-contact 3d coordinate measurement systems. Measurement 2019;151:107–20.
[38] Lin J, Li X, Park W. Position-constrained calibration compensation for hand–eye of laser profilers. Sensors 2024;24(23):7554.
[39] Gautam S, Patel RBA, Sharma M. Streamlined robotic hand–eye calibration of multiple 2d profilers: a rapid closed-form two-stage method via a single-plane artefact. Robot Comput Integr Manuf 2025;92:102984.
[40] Putzer M, Pichler T, Schlager FS. Self-optimizing method and software for calibration of laser systems with mechanical and optical axes. Opt Lasers Eng 2024;171:107740.